Numerical modeling on strengthening mechanisms of the harmonic structured design on CP-Ti and Ti–6Al–4V

Xiang Wang, Jia Li, Fabien Cazes, Azziz Hocini, Guy Dirras

Numerical modeling on strengthening mechanisms of the harmonic structured design on CP-Ti and Ti-6Al-4V

Xiang Wang, Jia Li*, Fabien Cazes, Guy Dirras, Azziz Hocini

Université Paris 13, Sorbonne Paris Cité, Laboratoire des Sciences des Procédés et des Matériaux, CNRS UPR 3407, 93430 Villetaneuse, France

*Corresponding author: Prof. Jia Li; Email: jia.li.lpmtm@gmail.com;

Phone +33 1 49 40 28 89, Fax +33 1 49 40 39 38

Abstract: The present work investigates and compares the deformation mechanism of harmonic structured (HS) CP-Ti and Ti-6Al-4V alloy to that of homogeneous coarse-grained (CG) counterparts. A set of simple shear tests on homogeneous CG and HS specimens for CP-Ti and Ti-6Al-4V was conducted under monotonic and cyclic simple shear loading conditions. Efforts have been made to develop a numerical model which is aimed to investigate the microstructure-related mechanical behavior of the materials. Numerical and experimental results were confronted to confirm the validity of the proposed model. To better understand the strengthening mechanisms of the HS design, comparisons between HS CP-Ti and HS Ti-6Al-4V were conducted and discussed in terms of macroscopic stress-strain response and distribution of stress/strain fields. Furthermore, forecasting mechanical properties of HS CP-Ti and HS Ti-6Al-4V including various volume fractions of fine-grained (FG) regions were simulated by using the developed model. It was demonstrated that strengthening mechanisms of harmonic designed CP-Ti and Ti-6Al-4V structures are different. This result explains why the HS design induces superior strengthening effect on CP-Ti than on Ti-6Al-4V.

Keywords: Microstructure; Crystal plasticity; Harmonic structure; Ti-6Al-4V; Finite elements

1. Introduction

Grain refinement via microstructure manipulation is an efficient method to strengthen metallic materials. However, the fine-grained (FG) and ultrafine-grained (UFG) materials generally suffer from significant loss of ductility compared to their coarse-grained (CG) counterparts in spite of their high strength. As a result, materials with homogeneous FG or UFG

microstructure lack the improved strength-ductility combination, which is crucial in evaluating the performance of metals of interest.

To overcome the disadvantage of homogeneous FG/UFG materials, many researchers have attempted to propose approaches to construct heterogeneous microstructures, which exhibit high strength and proper ductility (Kang et al., 2016; Lu et al., 2014; Fang et al., 2011; Ma and Zhu, 2017; Tingaud et al., 2019; Langlois et al., 2019). Among those works, Ameyama and co-workers proposed a new microstructure called 'harmonic structure' (HS) (Fujiwara et al., 2010; Orlov et al., 2013). It's actually a bimodal microstructure, where an interwoven structure of fine-grained (FG) regions and separately distributed coarse-grained (CG) regions are deliberately arranged to create structural heterogeneity. Different from the conventional way of preparing bimodal microstructure materials, the HS manufacturing process is able to control the grain size, volume fraction and even spatial distribution of FG and CG regions, thus achieving reliable mechanical properties and performance.

However, the general deformation mechanisms of different harmonic structured materials are still under exploration up to now. Over the past decade, considerable effort has been put into the processing and characterization of HS materials. High strength with slight ductility loss has been reported in the experimental investigation of commercial-purity titanium within monotonic tensile tests (Vajpai et al., 2016a). The experimental observations in (Vajpai et al., 2016b) illustrated that the peculiar spatial arrangement of FG and CG regions in the HS Co-Cr-Mo promotes uniformity of strain distribution and suppresses the localized plastic deformation, thus leading to improved mechanical properties. Dirras and co-workers (2017) fabricated HS Ti-25Nb-25Zr β-titanium alloy and evaluated its mechanical properties through cyclic shear experiments in comparison with the homogeneous counterpart. For the HS Ti-25Nb-25Zr, it was reported that plastic incompatibilities because of grain size difference were accommodated through accumulating GNS appearing in the FG region/CG region vicinity. Kikuchi and co-workers (2018) studied the fatigue properties of harmonic structured Ti-6Al-4V and observed an improved fatigue resistance.

Although great progress has been achieved in applying the concept of harmonic structure design to different metals, it is clear that this progress is still insufficient for practical engineering needs. For the moment, as different materials generally have different complex microstructure features, such as spatial arrangement of grains and phases, slip system geometries or distribution

of grain sizes, etc., the fundamental mechanisms of deformation and strengthening of HS materials have not been well understood. This issue is of crucial importance in optimizing the microstructure design and quantitative prediction on mechanical properties. Theoretical and numerical modeling can play an important role in this material design optimization.

It was noticed that grain sizes and volume fractions of FG/CG regions have a direct influence on mechanical properties of HS materials. Zhang and co-workers performed research on HS SUS304L and SUS316L stainless steels (Zhang et al., 2014; Zheng et al., 2016), which depicted the dependence of material's strength and ductility on average size of all grains and the volume fraction of FG regions. The experimental study in (Vajpai et al., 2016a) on HS CP-Ti also revealed the combined effect of refined grain size and volume fraction of FG regions in material strengthening. Park and colleagues (2018) conducted research on deformation mechanism of HS 304L stainless steel by using the micro-digital image correlation (micro-DIC) technique to precisely measure the strain distribution. It was reported that the strain concentrations were detected near the FG/CG region boundaries and higher strain level was found in CG regions than in FG regions. In addition to these experimental studies, some numerical works have been carried out to investigate the deformation mechanism of a few HS materials. Liu and colleagues (2018) used a polycrystalline multi-scale approach to build a plasticity-damage finite element model for HS CP-Ti. The Hall-Petch relation was used to simulate the grain size effect of tensile specimens under monotonic loading. In a recent work (Wang et al., 2019) the hardening behavior of harmonic structured CP-Ti in cyclic shear tests was assessed by developing a crystal plasticity based numerical model. The strain concentration in the CG regions was well reproduced in the simulation. The numerical results indicate that the strength improvement of harmonic structured CP-Ti was chiefly caused by the FG regions.

Ti-6Al-4V is the most widely used titanium alloys in lots of industrial applications by virtue of its excellent combination of high strength, corrosion property, ductility, and low weight. Inspired by the work of Kikuchi and colleagues (2018), according to which the HS Ti-6Al-4V showed a higher fatigue resistance, we carried out a similar investigation on HS Ti-6Al-4V, attempting a better strength-ductility combination under monotonous and cyclic loading. However, the mechanical tests showed that the improvement is not as significant as expected, contrariwise to the remarkable performance of HS CP-Ti. Therefore, besides microstructure specificities, the strengthening effect of the HS design should be different for these two metals.

Therefore, the main motivation of the present work is to better understand these mechanisms by means of a detailed numerical investigation.

This work is focused on understanding the general deformation mechanism of HS materials by performing numerical simulations of strengthening behavior under monotonous and cyclic simple shear loading condition for two typical materials, namely CP-Ti and Ti-6Al-4V. To this end, a new approach combining a crystal plasticity model for lamellar α+β colonies (Mayeur, 2004) with the numerical model developed in authors' recent work (Wang et al., 2019) has been explored and implemented.

In Section 2 of this paper, two sets of monotonous and cyclic simple shear tests on homogeneous coarse-grained and harmonic structured CP-Ti and Ti-6Al-4V are presented. The characteristics of microstructure for all specimens and the measurement of key microstructure lengths are also described in this section. Section 3 describes the crystal plasticity model for lamellar α+β colonies and for equiaxed α phases as well as the scale transition rule to develop a numerical model which can be used to simulate the deformation behavior of HS CP-Ti and HS Ti-6Al-4V. Section 4 demonstrates details of numerical simulations including the used slip systems, the identification procedure of model parameters and a set of finite element model validations for specimens. Section 5 presents comparisons of numerical and experimental results and comparisons of simulated deformation behaviors between CP-Ti and Ti-6Al-4V. The emphasis is on the discussion of the deformation mechanism of HS CP-Ti and HS Ti-6Al-4V as well as the general strengthening mechanism of HS materials. Finally, some conclusions are made in Section 6.

2. Materials and experiments

The study of general deformation mechanism of HS materials requires the combination of experimental and numerical research on different materials, thus CP-Ti and Ti-6Al-4V are chosen for the experiments due to the typical microstructures of their HS and homogeneous CG specimens.

Plasma Rotating Electrode Process (PREP) has been applied to fabricate the CP-Ti and Ti-6Al-4V powders whose average particle size was about 140μm and 180μm respectively. The amount of titanium in CP-Ti is 99.81% (wt%). The chemical composition (wt%) of Ti-6Al-4V powders is as follows: Al(6.51) V(4.26) O(0.18) Fe(0.17) C(0.01) N(0.003) H(0.002) Ti(balance). To produce bulk HS CP-Ti and Ti-6Al-4V specimens, the PREP powders were further processed

by mechanical milling (MM) in a planetary ball mill at room temperature under argon gas atmosphere for 100 hours and 25 hours respectively. To make the bulk CP-Ti material, the as-PREP powders and MM powders were consolidated respectively by spark plasma sintering (SPS) at 1073K (800℃) under vacuum atmosphere for 10 min. While for Ti-6Al-4V, the SPS condition was adjusted to 1123K (850℃) and 30 min. More information about the processing techniques can be found in (Ota et al., 2014a, 2014b). Three methods, namely SEM, EBSD and Energy-dispersive X-ray spectroscopy (EDS) are used to provide microstructural information for numerical study.

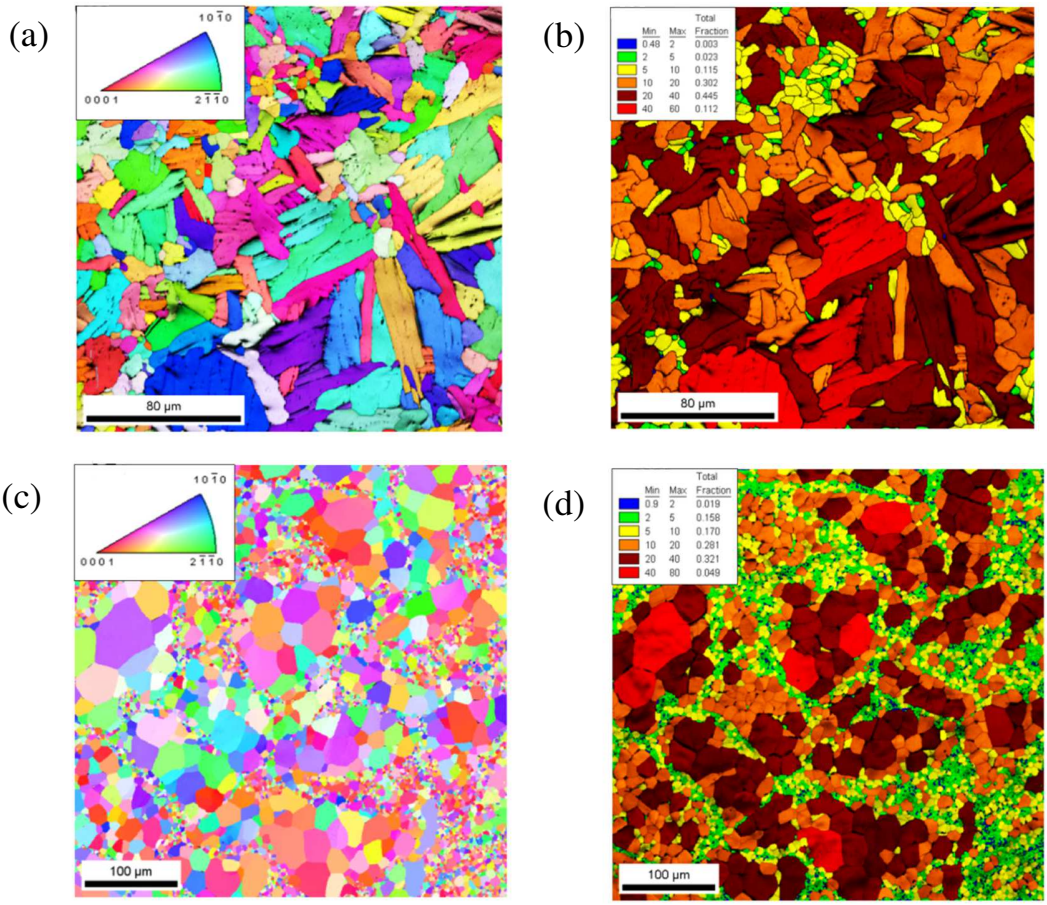

Figure 1. Figures of the as-processed specimens: (a) and (c) IPF maps showing grain orientation ([0001] projection) for homogeneous coarse-grained CP-Ti and harmonic structured CP-Ti, respectively. The color code is relative to the standard stereographic projection triangle (inset); (b) and (d) figures showing the grain sizes and their distribution for homogeneous coarse-grained CP-Ti and harmonic structured CP-Ti, respectively (Hocini, 2017).

The microstructures of HS and homogeneous samples are analyzed by scanning electron microscopy (SEM) coupled with EBSD analysis. For CG CP-Ti, Figure 1b shows that the microstructure is quite 'homogeneous' with an average grain size of approximately 25µm. In

comparison, HS CP-Ti exhibits a specific bimodal microstructure where FG regions (with an average grain size of 5μm) form an interconnected 3D network surrounding CG regions (with an average grain size of 30μm), seen in Figure 1d. The volume fraction of FG regions is computed to be about 16.0%. Figures 2a and 2b show that the microstructure of the investigated homogeneous CG Ti-6Al-4V is characterized by the lamellar α+β colonies where the β phase lamellas are embedded in α phase transformation structures. In Figures 2c and 2d harmonic microstructure can be clearly observed for HS Ti-6Al-4V. However, FG regions are mainly composed of relatively small equiaxed α phase grains and CG regions mainly consist of lamellar α+β colonies, thus significantly adding complexity to the microstructure.

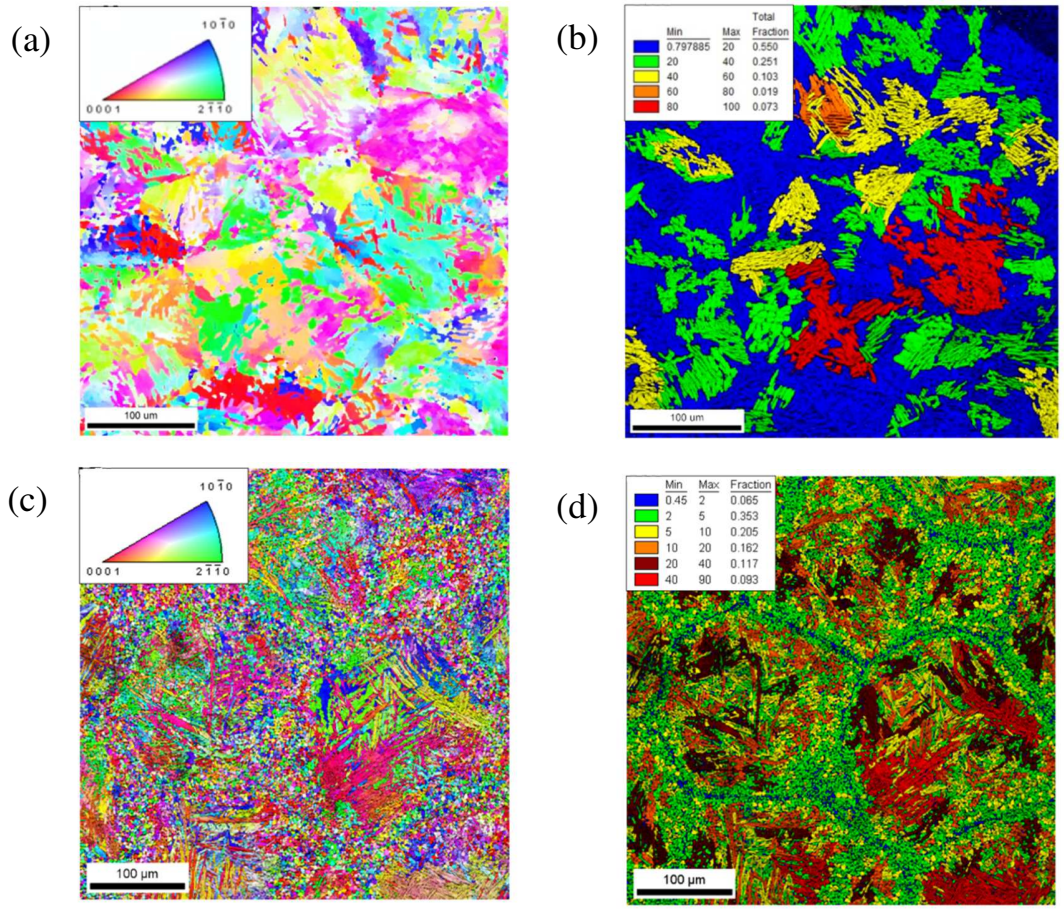

Figure 2. Figures illustrating the microstructural of the as-processed specimens: (a) and (c) IPF maps showing grain orientation ([0001] projection) for homogeneous coarse-grained Ti-6Al-4V and harmonic structured Ti-6Al-4V, respectively. The color code is relative to the standard stereographic projection triangle (inset); (b) and (d) figures showing the grain sizes and their distribution for homogeneous coarse-grained Ti-6Al-4V and harmonic structured Ti-6Al-4V, respectively (Hocini, 2017). Notice the grain size gradient in the fine-grained regions (blue ≈0.45-2 μm; green ≈2-5 μm).

The identification of key microstructure length scales is directly dependent on the microstructure characterizations. For Ti-6Al-4V specimens, the average size of the lamellar colony is assumed to equal to the average length of α laths. EDS is applied to measure the relative abundance of presented chemical elements in α lath and β lath respectively. This method provides clearer microstructure images, permitting a convincing and precise measurement of the average widths of α and β laths, as shown in Figure 3. For the homogeneous CG Ti-6Al-4V, the measured average lamellar α+β colony size, widths of α lath and β lath are 49.4 μm, 2.5 μm and 0.2 μm. For the HS Ti-6Al-4V, the volume fraction of FG regions is 13.34% and the average grain size of equiaxed α phase is 2.05 μm. Based on experimental identification, the lamellar α+β colonies in CG regions can be assumed to have the same microstructure lengths as measured for homogeneous CG Ti-6Al-4V.

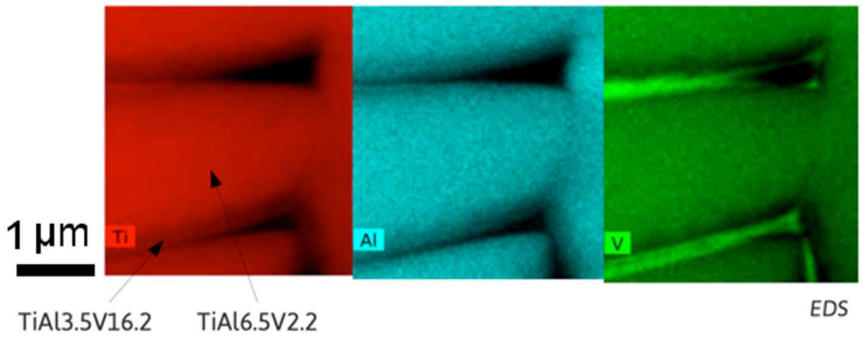

Figure 3. EDS map showing the relative abundance of chemical elements in α lath and β lath.

Mechanical properties were studied by performing mechanical tests for the four kinds of specimens under monotonous and cyclic simple shear loading on an MTSM20 testing apparatus with a shearing device. The samples are cylindrical plates of 20 mm in diameter and 1 mm in thickness with $15 \times 2 \times 1 mm^3$ effective sheared volume. The imposed shear strain is controlled by $\Gamma = s/l$, where s is the displacement of the grip, $l = 2.0mm$ represents the width of shear zone. A constant strain rate of $10^{-3}s^{-1}$ was used in the loading procedure. Monotonous simple shear tests were conducted for all specimens. Cyclic simple shear experiments accompanying imposed increasing overall strain amplitudes were also performed. The increment of the overall strain amplitudes in cyclic shear tests was $\Delta\Gamma = 1.155\%$ per cycle.

The obtained engineering stress-strain curves are shown in Figure 4 and Figure 5. Results for CG samples and HS samples are shown in the same figure in order to emphasis the strengthening effect of the HS design. Following remarks can be made from these figures:

1. The application of the harmonic structure design on both CP-Ti and Ti-6Al-4V improves the material strength in comparison with their homogeneous CG counterparts, in both the monotonous and cyclic shear tests.

2. However, the increase of Ti-6Al-4V's strength resulting from the effect of harmonic structure design is less significant than that of CP-Ti. When monotonic loading imposed, the strength of the HS CP-Ti increase more than 25% with respect to the homogeneous CG counterpart, while only about 7% is gained for HS Ti-6Al-4V specimens. Under cyclic loading, this comparison is about 25% vs. 15%. In terms of absolute values, the strength increase provided from the HS design is twice bigger for CP-Ti than for Ti-6Al-4V under monotonic loading. Under cyclic the absolute increases are similar for the both metals.

In the following sections, the above-obtained experimental results will be analyzed by developing a 3D numerical model with which detailed numerical simulations were carried out.

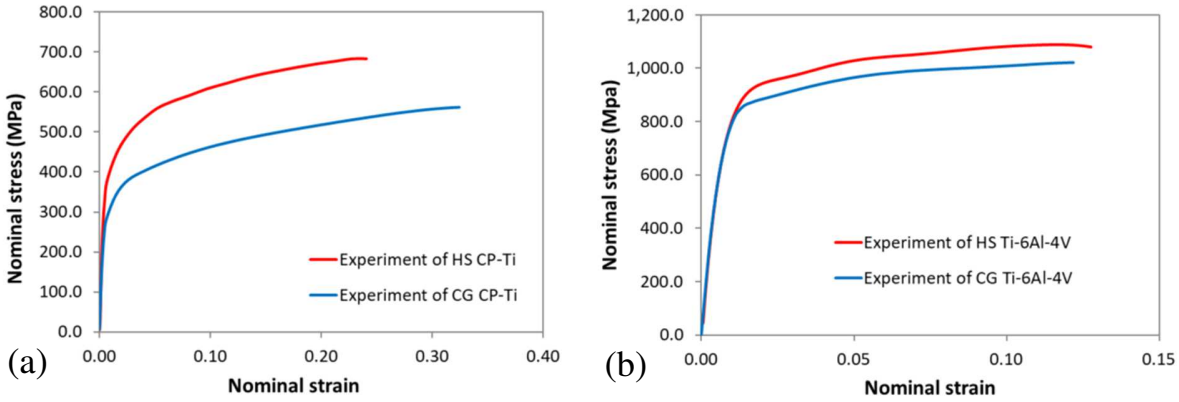

Figure 4. Experimental results for (a) harmonic structured CP-Ti and homogeneous coarse-grained CP-Ti, (b) HS Ti-6Al-4V and homogeneous CG Ti-6Al-4V in the case of monotonic simple shear condition.

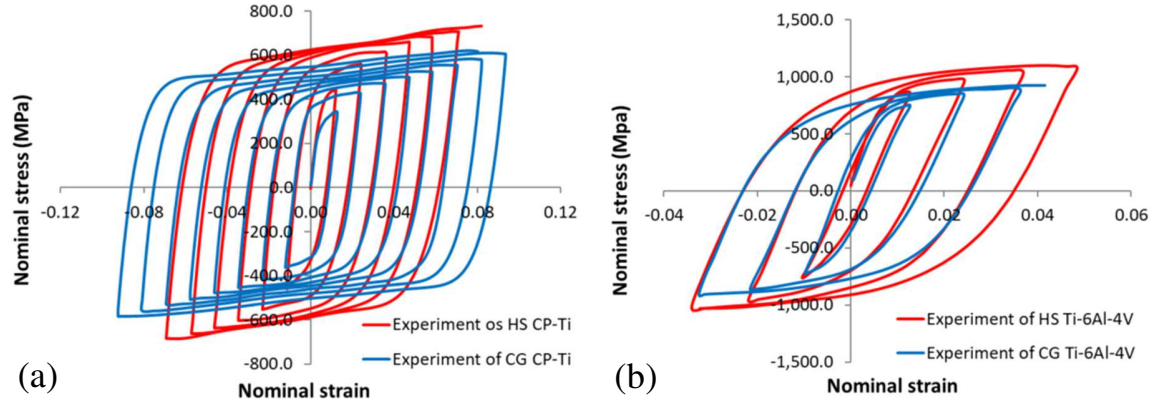

Figure 5. Experimental hysteresis loops for (a) harmonic structured CP-Ti and homogeneous coarse-grained CP-Ti, (b) harmonic structured Ti-6Al-4V and homogeneous coarse-grained Ti-6Al-4V in the case of cyclic simple shear condition when $\Delta\Gamma$=1.155% every cycle.

3. Simulation methods

3.1 General consideration

In numerical simulations, Voronoi's tessellations are regarded as an efficient method to generate random polycrystals (Barbe et al., 2001). However, direct meshing of individual grains or α+β colonies for HS Ti-6Al-4V results in a representative volume element including an extremely huge number of elements due to the huge contrast between the grain sizes in FG and CG regions, leading to thus an impractical and inefficient finite element (FE) model. To overcome this difficulty, a scale transition rule is necessary to develop a realistic 3D numerical model. Among the multi-scale transition methods, the concept of self-consistent framework has proven to be a good candidate to predict the intergranular heterogeneity, where an individual grain is regarded as an inclusion in a homogeneous medium which has the average properties of the polycrystals. In this work, an explicit self-consistent method, called 'β-rule' developed by Cailletaud (1987) and reshaped by Pilvin (1990), was employed in our numerical model. Therefore, the direct meshing of a large number of grains for HS Ti-6Al-4V is averted and the gigantesque computation task is significantly reduced.

To implement the proposed numerical model in simulating the behavior of HS materials, three operating levels can be defined according to the scale on which the deformation is described by the constitutive relations. The scale of RVE is regarded as the first level where a sufficient number of coarse grained regions and interconnected network of fine grained regions are

considered. And at this scale, the macroscopic responses in terms of stress and strain are assumed to follow the linear elastic relation. The second level called mesoscopic level is then defined at each continuum point. The number of grains contained at every Gauss point is determined through either the convergence test or the microstructure characterization result. Here the 'β-rule' is used to calculate local stresses of the underlying grains from the macroscopic stresses of Gauss points. With respect to the plastic strain, the macroscopic plastic strains are estimated from the granular plastic strains through a homogenization procedure. Finally, the plasticity development is estimated at the third level corresponding to the scale of crystallographic slip system (CSS). Crystal plasticity is applied at this level to relate slip activities to resolved shear stresses on all slip systems. The implementation of the scale transition rule 'β-rule' is then fulfilled and the three operating levels are depicted in Figure 6.

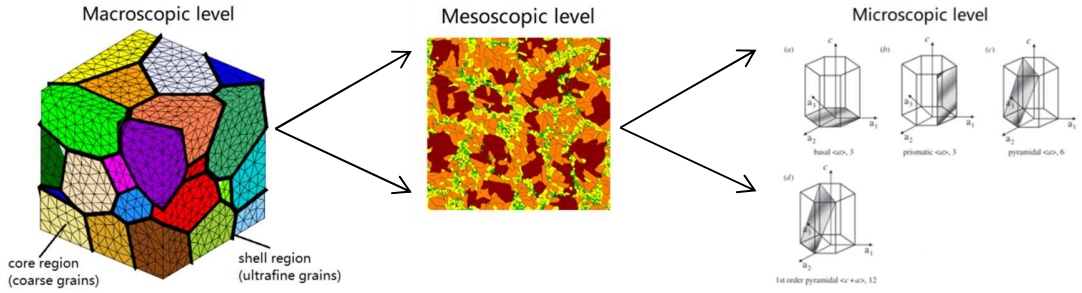

Figure 6 Images showing the implementation of 'β-rule' in the present numerical model.

Another difficulty is the complex microstructure of Ti-6Al-4V with lamellar colonies. In addition to employing the high fidelity finite element modelling in which the α phase and the β phase in lamellar α+β colonies are explicitly represented by using fin finite element mesh (Obstalecki et al., 2014; Kasemer et al., 2017), an efficient alternative is to construct equivalent slip geometry of multi-phase materials with the help of simplified representations of microstructures (Morrissey, 2001; Goh et al., 2001, 2003; Schoenfeld et al., 2002; Mayeur et al., 2007). Goh et al. (2001) made use of a 2D planar triple slip idealization where the 3D slip geometry was simplified to three active slip systems representing deformation only by prismatic slip. Schoenfeld et al. (2002) also employed a planar triple slip idealization with one system representing prismatic slip and two systems representing idealized pyramidal slip. However, such models are incapable of modeling the full spectrum of realistic textures that are commonly attained in Ti-6Al-4V polycrystals. The construction of a 3D constitutive model is of significant importance to study the effects of a wide range of orientation distributions, 3D slip systems and

slip system anisotropy on deformation behavior. Direct meshing of such a complex microstructure must contain a great many of grains, and therefore is extremely costly. In the present study, a 3D crystal plasticity model (Mayeur and McDowell, 2007), which can be referred as equivalent constitutive model (ECM), is adopted. The ECM integrates the slip systems of α and β phases of a laminar $\alpha + \beta$ colony into an equivalent super grain by following certain geometrical relationships, named as the Burgers orientation relation (BOR). The consequence of this lamellar structure and the BOR is that certain deformation modes are considered as "hard" when the slip directions intersect the α/β interface due to the relatively small effective slip distance and other deformation modes are considered as "soft" when the slip systems slide parallel to the α/β interface or bear parallel slip planes in both phases.

By using the ECM, there is no need to explicitly mesh the individual lamellae in a FE model. The microstructural aspect of the ECM is briefly presented in Appendix 1. More details of this model can be found in the original work of Mayeur (2004).

The global scheme of the numerical calculations is as follows:

For CG CP-Ti and Ti6Al4V, polycrystalline RVEs are built by means of Voronoi's tessellation with a large number of grains for CG CP-Ti, or α + β colonies for CG Ti-6Al-4V. Crystal plasticity theory is used to establish the constitutive laws. Besides, polycrystalline models are also used to verify the validity of the β-rule by applying this rule to a homogeneous RVE.

For HS CP-Ti and HS Ti-6Al-4V, the Voronoi tessellation technique is used for the RVE's formation. CG regions and FG regions are separately meshed. At each Gauss point, a large number of grains are considered for HS CP-Ti while only a finite number of α + β colonies are examined for HS Ti6Al4V in order to establish the corresponding constitutive law. The β-rule is used as a homogenization-localization procedure for macro-micro stress/strain transition.

3.2 Constitutive model

In the framework of the large deformation plasticity, the total Green-Lagrange strain tensor $\boldsymbol{E}$ can be split as the sum of an elastic part $\boldsymbol{E}^e$ and a plastic part $\boldsymbol{E}^p$. At the macroscopic level, the elastic portion of deformation is assumed to obey a linear elastic constitutive relationship, namely:

$$\boldsymbol{T} = \boldsymbol{C}\boldsymbol{E}^e = \boldsymbol{C}(\boldsymbol{E} - \boldsymbol{E}^P) \tag{1}$$

where $\boldsymbol{C}$ is the elastic stiffness tensor, and $\boldsymbol{T}$ is the second Piola-Kirchhoff stress tensor. The stress measure is Cauchy stress $\boldsymbol{\sigma}$ which can be deduced from the second Piola-Kirchhoff stress $\boldsymbol{T}$ as:

$$\boldsymbol{\sigma} = \frac{1}{\det \boldsymbol{F}} \boldsymbol{F}\boldsymbol{T}\boldsymbol{F}^{\boldsymbol{T}} \tag{2}$$

where $\boldsymbol{F}$ is the deformation gradient tensor. The yield function used in this work for each slip system is chosen as (Chaboche, 1989):

$$f^i = \left|\tau^i - \chi^i\right| - R^i - k^i \tag{3}$$

where i represents the slip system, χ^i indicates the back stress, τ^i denotes the resolved shear stress, k^i is the threshold stress representing the initial yielding, R^i being its evolution. A rate dependent formulation is employed to describe the relationship between the plastic slip rate of slip systems and the resolved shear stress. The flow rule calculating the plastic slip rate $\dot{\gamma}^i$ of slip system i is given by:

$$\dot{\gamma}^i = \dot{\gamma}_0 \langle \frac{f^i}{D^i} \rangle^m sgn\left(\tau^i - \chi^i\right) \tag{4}$$

where $\dot{\gamma}_0$ denotes the reference shearing rate, D^i is the drag stress representing the slip resistance, m describes the strain-rate sensitivity, $sgn\left(\tau^i - \chi^i\right)$ represents the direction of plastic flow. Slip activity can only appear when the stresses are above the threshold for all slip systems.

For each slip system i, whose slip direction vector and slip plane normal vector are l^i and n^i respectively, the corresponding resolved shear stress τ^i can be calculated as:

$$\tau^i = \boldsymbol{\sigma}^{\boldsymbol{g}} : \boldsymbol{m}^i \tag{5}$$

with

$$\boldsymbol{m}^i = \frac{1}{2}\left(l^i \otimes n^i + n^i \otimes l^i\right) \tag{6}$$

The back stress is assumed to evolve as a nonlinear Armstrong-Frederick direct hardening / dynamic recovery type relationship (Mayeur and McDowell, 2007):

$$\dot{\chi}^i = B\dot{\gamma}^i - C\chi^i\left|\dot{\gamma}^i\right| \tag{7}$$

According to (Chaboche, 1989), isotropic hardening is the governing factor to influence the cyclic hardening. Then a phenomenological isotropic hardening rule is applied:

$$\dot{R}^i = a\left(Q - R^i\right)\left|\dot{\gamma}^i\right| \tag{8}$$

Where R^i is isotropic hardening variable, Q stands for its saturation, a denotes the isotropic hardening modulus.

The threshold stress k^i is closely related to the free slip length of each slip. Thus a Hall-Petch type relationship is used to assess the scale effects:

$$k^i = k_0(1 + k_y(d^i)^{-0.5}) \tag{9}$$

where k_0 is a referential critical resolved shear stress, k_y is fixed coefficient. d^i is the characteristic microstructure length. For CP-Ti specimens, d^i denotes the grain sizes of equiaxed α phases. While when simulating Ti-6Al-4V specimens, the d^i values with respect to α+β colonies correspond to either the colony size, the α lath width or the β lath width.

The main source of intergranular heterogeneity is related to a phenomenological variable $\boldsymbol{\beta^g}$ which is able to correctly capture the plastic accommodation (Cailletaud and Pilvin, 1994). The granular stress tensor σ^g is determined by:

$$\boldsymbol{\sigma^g} = \boldsymbol{\sigma} + C^g(\boldsymbol{B} - \boldsymbol{\beta^g}) \tag{10}$$

$$\boldsymbol{B} = \sum_{g=1}^{G} f^g \boldsymbol{\beta^g} \tag{11}$$

where $\boldsymbol{B}$ is the mean of variable $\boldsymbol{\beta^g}$ for all grains, g represents the equiaxed α grains or lamellar α+β colonies, G indicates all grains (or colonies) considered at a continuum point, C^g denotes a material parameter, f^g denotes the volume fraction for every grain (or every colony). The evolution of $\boldsymbol{\beta^g}$is calculated through a differential equation (Cailletaud and Pilvin, 1994):

$$\dot{\boldsymbol{\beta}}^g = \dot{\boldsymbol{E}}^{gp} - C_\beta \boldsymbol{\beta}^g \sum_{i=1}^{tot} \left|\dot{\gamma}^i\right| \tag{12}$$

where C_β denotes a material parameter, $\dot{\boldsymbol{E}}^{gp}$ represents the granular plastic strain rate, *tot* denotes the corresponding total number of slip systems in the slip geometry, the summation is over the slip systems *i* of the grain *g* (or colony *g*).

When dealing with equiaxed α phases, the plastic deformation rate at the grain level $\dot{\boldsymbol{E}}^{gp}$ is a linear summation of all activated slip systems described by the symmetrical part of the Schmid tensor in the slip geometry:

$$\dot{\boldsymbol{E}}^{gp} = \sum_{i=1}^{tot} \dot{\gamma}^i \, \boldsymbol{m}^i \tag{13}$$

When dealing with the lamellar α+β colony, the granular plastic deformation rate $\dot{\boldsymbol{E}}^{gp}$ should be calculated through an equation considering the average volume fractions of α and β phases for lamellar α+β colonies:

$$\dot{\boldsymbol{E}}^{gp} = v^{\alpha} \sum_{i=1}^{s} \dot{\gamma}^i \, \boldsymbol{m}^i + v^{\beta} \sum_{l=1}^{t} \dot{\gamma}^l \, \boldsymbol{m}^l \tag{14}$$

where v^{α} and v^{β} denote the respective volume fractions of α and β phases and are in direct proportion to their widths, s is the total number of the slip systems corresponding to hcp slip geometry, t is the total number of the slip systems corresponding to bcc slip geometry, and $s + t = tot$. The macroscopic plastic strain rate can be estimated as the weighted average of the granular plastic strain rate as follows:

$$\dot{\boldsymbol{E}}^{p} = \sum_{g=1}^{G} f^g \, \dot{\boldsymbol{E}}^{gp} \tag{15}$$

4.0 Numerical simulations

4.1 Slip systems

There are 24 HCP slip systems considered in the model for equiaxed α phase. And for lamellar α+β colonies, 36 slip systems are considered to form the equivalent slip geometry including 24 HCP slip systems and 12 BCC slip systems. These slip systems are shown in Table A1. It is noticed that both the BCC slip systems and 12 $\langle c + a \rangle$ first-order pyramidal $\{10\bar{1}1\}\langle 11\bar{2}3\rangle$ are able to give needed degrees of freedom to accommodate plastic deformation along $(0001)_{\alpha}$ direction in the equivalent slip geometry of lamellar colonies. Besides, deformation twinning is very rare and consequently is not considered in the present model. According to the inverse pole figure (IPF), no preferential grain orientation is observed. For the sake of brevity, only the analysis on IPF data of harmonic structured Ti-6Al-4V is presented as an example. It can be seen in Figure 7 that the maximum pole density is quite low (about 1.6). The same results same have been observed for other samples since the high temperature fabrication process used is the same. Therefore, the Euler angles which represent the grain orientations for both CP-Ti and Ti-6Al-4V can be considered as randomly distributed.

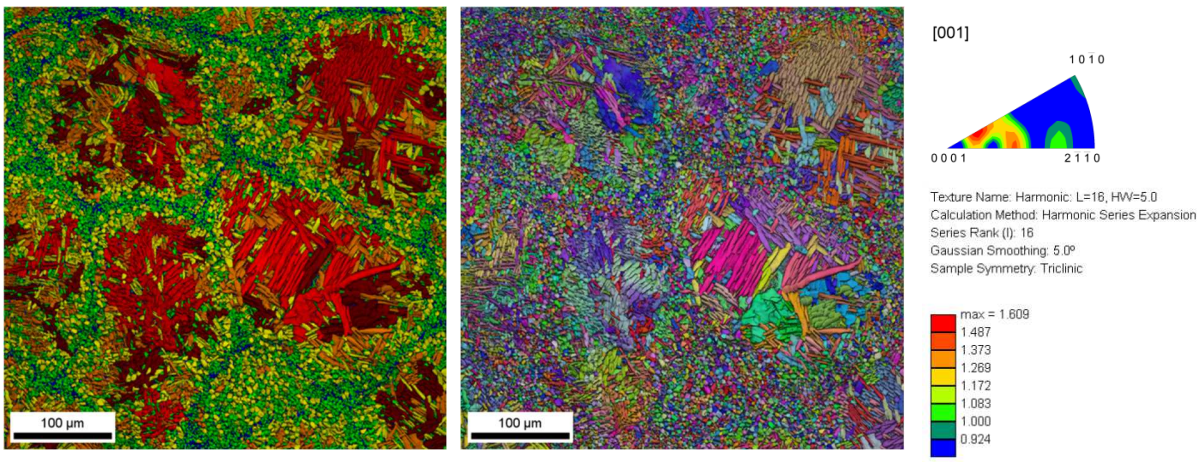

Figure 7. Grain size (left) and IPF (middle) maps, alongside the texture strength measurement (right) for the as-processed harmonic structured Ti-6Al-4V. Texture strength is expressed by the scale level at the bottom of (c).

4.2 Parameter determination

Model parameters describing the crystal plasticity properties and the scale transition can be gathered from the literature or identified by the experimental tests. Due to the inherent difference between CP-Ti and Ti-6Al-4V, some parameters have to be identified on the basis of their respective mechanical tests. Experimental data of monotonous shear tests for homogeneous coarse-grained specimens and harmonic structured specimens and the cyclic shear tests with $\Delta\Gamma = 1.155\%$ for homogeneous CG specimens were emplyed to determine the model parameters. Whereas the data from the cyclic shear tests with $\Delta\Gamma = 1.155\%$ for HS specimens were then used to examine the performance of the numerical models with the calibrated parameters.

For Ti-6Al-4V, the value of Young's modulus measured according to our experiments is akin to that in the work (Simmons et al., 1971). For CP-Ti, the Young's modulus was set equal to that of Ti-6Al-4V and the value was also close to the measurement reported in the work of Seagle (1997). The approximate value of k_y was first determined by referring to that reported in (Liu et al., 2019) in which they identified the parameter as 3.8 based on experimental studies presented in ((Naka and Lasalmonie, 1983; Naka et al., 1988). By fitting the yield strength of monotonic shear tests for CG CP-Ti and HS CP-Ti samples, a new value for k_y which was readjusted from the approximate value and the value of k_0 were estimated. Afterwards, these two parameters were tested again and slightly changed by fitting the cyclic shear test. The same procedure was then repeated for CG Ti-6Al-4V and HS Ti-6Al-4V samples to identify the coefficients k_0 and k_y.

The values of $\dot{\gamma}_0$ and m in the flow rule were gathered from different literatures, i.e., from the work of Kasemer and colleagues (2017) for Ti-6Al-4V and from the study (Hama et al., 2017) for CP-Ti, respectively. Parameters related to isotropic hardening and kinematic hardening, namely C, B, Q and a, were calibrated by fitting the monotonic hardening and cyclic hardening of homogeneous CG specimens for CP-Ti and Ti-6Al-4V respectively. The values of the slip strengths D^i for different slip systems were determined by referring to the work of Song and colleagues (2008) and akin to those listed in the articles (Yang et al., 2011). The slip strength of bcc slip systems was set equal to that of the basal systems of the hcp slip systems.

For CP-Ti, the values of parameters C^g and C_β are determined by referring to Barkia's work (2014) which is based on his experiments about single crystal titanium. However, due to the lack of direct reference in the literature, the parameters C^g and C_β for Ti-6Al-4V were identified by fitting the numerical overall response of monotonous shear test obtained by polycrystalline simulation for homogeneous CG Ti-6Al-4V.

The calibrated values of the used parameters are listed in Table 2.

Table 2

Model parameters used in this work.

Parameter	Value		Parameter	Value	
	CP-Ti	Ti-6Al-4V		CP-Ti	Ti-6Al-4V
D^{basal}(MPa)	353	353	m	50.0	9.0
D^{prism}(MPa)	397	397	$\dot{\gamma}_0(s^{-1})$	0.001	1.0
$D^{pyr<a>}$(MPa)	441	441	Q(MPa)	207.0	50.0
$D^{pyr<c+a>}$(MPa)	503	503	a	14.5	2.0
D^{bcc}(MPa)	-	353	B(MPa)	815.0	2070.0
E(GPa)	106.0	106.0	C	10.0	5.0
ν	0.3	0.3	C_β(MPa)	65.5	0.0
k_0(MPa)	40.7	48.0	C^g(GPa)	45.0	15.0
$k_y(\mu m^{0.5})$	4.4	5.15			

4.3 Finite element model tests

Finite element model tests for homogeneous CG and HS specimens are performed to investigate the reliability of the proposed numerical model. These model tests are all based on the monotonous simple shear experiments described in Section 2. The boundary condition is schematically shown in Figure 8, where the planned displacements are imposed on all surfaces of RVEs.

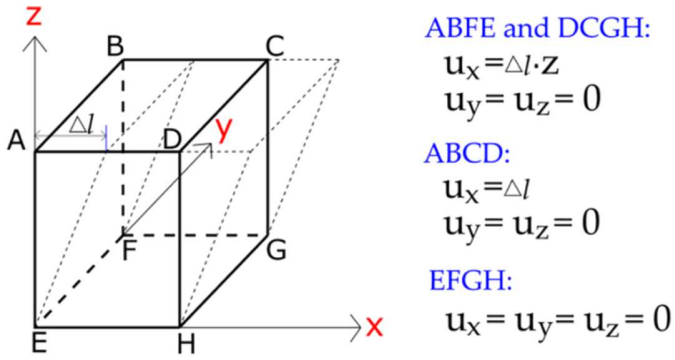

Figure 8. Illustration of the boundary conditions of simple shear loading used in this work.

To better simulate the mechanical responses of the investigated materials, namely, homogeneous coarse-grained CP-Ti and harmonic structured CP-Ti, an array of FE model tests are conducted to determine the proper RVEs in a way similar to that described in (Wang et al., 2019). A balance must be found during the construction of a representative microstructure between two opposite requirements (i) having a sufficiently large number of grains or CG regions to get a reasonable description of the local heterogeneity and to preserve the macroscopic isotropy of the RVE, (ii) reducing the time and memory cost to make the simulation computationally feasible. This allows us to efficiently carry out the computation with sufficient reliability. To this end, we carried out numerical tests by doubling successively the value of such a parameter, the number of grains, for example. When the discrepancies between the macroscopic stress-strain curves do not exceed 2.5%, we considered that the convergence is achieved.

The details of numerical tests with respect to CP-Ti material can be found in (Wang et al., 2019) and are not repeated for the sake of brevity. The microstructure parameters thus optimized for homogeneous coarse-grained CP-Ti and harmonic structured CP-Ti are presented in Figure 9 together with the generated RVEs. Here only the procedures of numerical tests on Ti-6Al-4V specimens are presented in the following.

Due to the lack of existing approach to generate finite element mesh for harmonic structured materials, authors developed an algorithm based on the Voronoi tessellations. The developed algorithm is able to construct many random coarse-grained regions surrounded by an interconnected 3D network of fine-grained regions whose thickness can be easily changed to control the volume fraction. However, the drawback of the developed algorithm is the faces of the generated RVE are slightly uneven. These slightly uneven surfaces have no influence on the accuracy of the numerical simulations as homogeneous strain boundary conditions are imposed on the contour by imposing a displacement vector $\boldsymbol{u}$ in the form of $u_i = E_{ij}x_j, x_j \in \partial\Omega$, where $\boldsymbol{E}$ is the average strain tensor and $\partial\Omega$ represents the RVE's boundary.

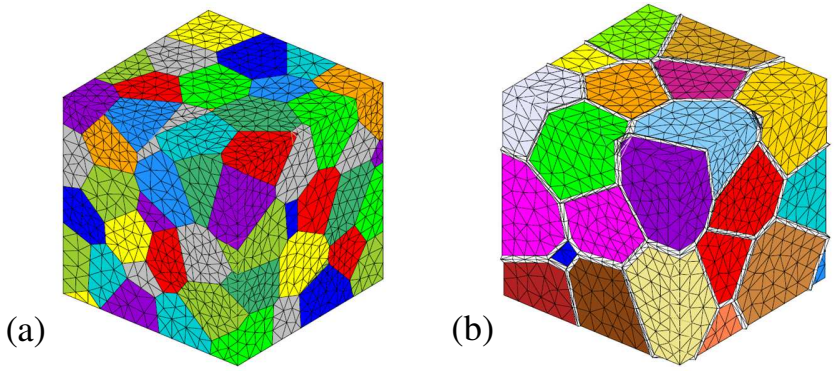

Figure 9. Illustration of the used RVEs in the present work for (a) homogeneous coarse-grained CP-Ti, where every color indicates an individual grain and 100 equiaxed α grains are included, and (b) harmonic structured CP-Ti, where 30 CG regions (colorful parts) are generated and 30 equiaxed α grains are considered at each Gauss point, white part represents FG regions.

When dealing with simulations of Ti-6Al-4V specimens, a cubic RVE of dimension of 1.0×1.0×1.0mm for homogeneous CG Ti-6Al-4V is constructed by using the Voronoi tessellation technique, as shown in Figure 10, which contains 50 arbitrary shaped lamellar α+β colonies with random grain orientations. Here the ECM is implemented in the simulation under the framework of CPFEM. As shown in the figure, each colored region denotes an equivalent grain which essentially represents a lamellar α+β colony. By using ECM, the fine details of alternating laths of α phase and β phase are not necessary to be explicitly represented, which significantly simplifies the construction of representative geometry and makes the simulations in 3D cases more feasible. Ten polycrystalline simulations with ten sets of randomly distributed grain orientations are carried out under simple shear loading conditions. The overall stress-strain curves corresponding to the ten simulations are shown in Figure 11, where the grain orientation effect to

the predicted mechanical performance is observed. However the variation of the overall responses remains reasonably low, thus it's reasonable to employ the polycrystalline FE mesh including 50 lamellar α+β colonies as a RVE for homogeneous CG Ti-6Al-4V.

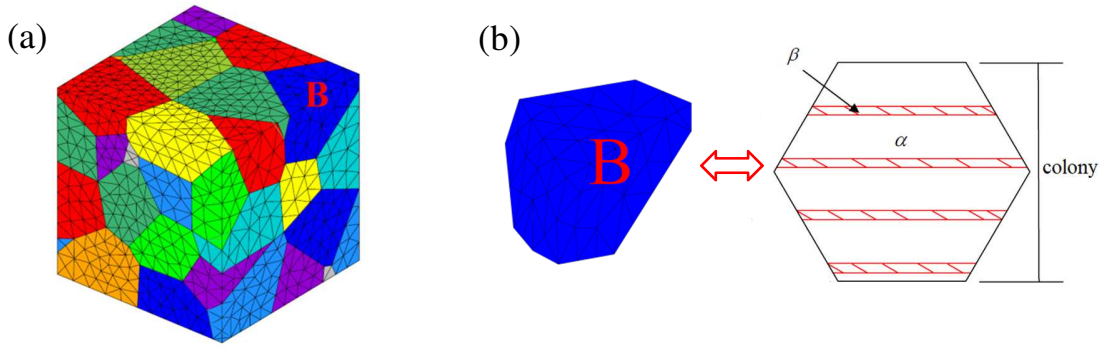

Figure 10. Illustration of (a) the RVE for homogeneous coarse-grained Ti-6Al-4V, where every colored region is an equivalent grain representing a lamellar α+β colony as shown in (b), and 50 lamellar α+β colonies are created.

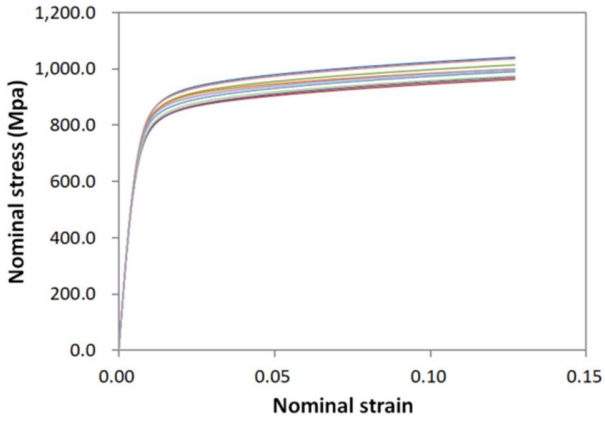

Figure 11. Simulated overall stress-strain curves under monotonic simple shear loading corresponding to ten sets of random grain orientations.

The previous simulated overall response of polycrystalline simulation for homogeneous CG Ti-6Al-4V is taken as a reference to test the performance of 'β-rule' and then calibrate the related parameters, namely C^g and C_β. In this model test, we use a cubic RVE of dimension of $1.0 \times 1.0 \times 1.0mm$ with 125 cubic elements, as shown in Figure 12a. One of the ten sets of random grain orientations and the corresponding volume fractions of the 50 lamellar α+β colonies are extracted from the previous polycrystalline simulation and then input into the UMAT programmed for the proposed numerical model. Consequently, the FE model in Figure 12a can be regarded as a homogenized counterpart of the polycrystalline FE model in Figure 10a. It's clear that the proposed numerical model which has incorporated the ECM and 'β-rule' makes it

unnecessary to directly mesh the fine details of aggregate of lamellar α+β colonies, thus making it feasible to construct the FE meshes for CG regions in HS Ti-6Al-4V.

The values of material parameters describing the crystal plasticity properties will remain the same as that in the previous polycrystalline simulation. And only parameters C^g and C_β need to be identified by fitting the overall response obtained in the previous polycrystalline simulation using the same set of random grain orientation. In Figure 12b, it can be seen that the obtained overall responses matches well with each other when the parameters C^g and C_β are calibrated as 15.0 GPa and 0.0 MPa respectively. We can remark that the ECM coupled with 'β-rule' reproduces faithfully the overall response obtained by polycrystalline simulation.

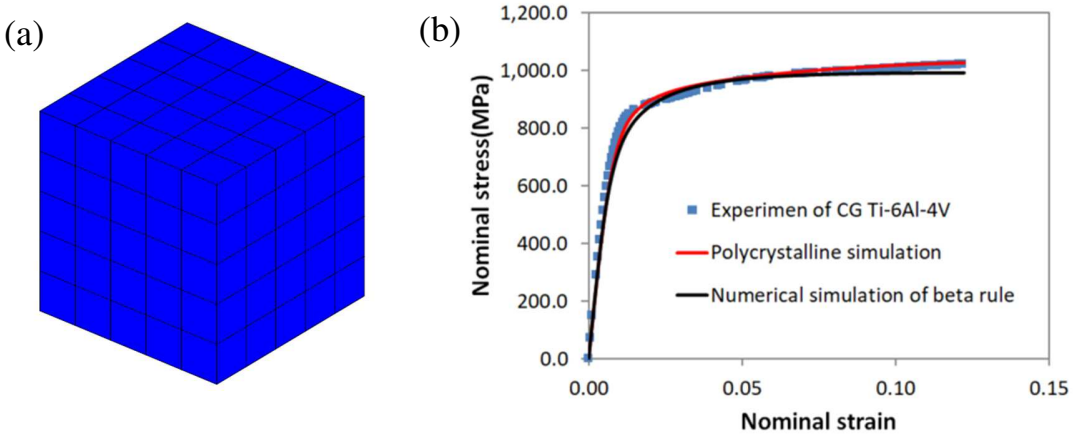

Figure 12. (a) Illustration of FE mesh used in the test of β-rule, (b) Numerical results obtained by FE model test for β-rule and polycrystalline simulation and the comparison with experimental data for homogeneous CG Ti-6Al-4V under monotonic simple shear loading condition.

After the validation of the proposed numerical model as mentioned above, FE model tests are carried out to determine a reasonable RVE to simulate the mechanical properties of HS Ti-6Al-4V. Based on the Voronoi tessellations, a method is developed to generate a microstructure which can represent the geometric features of FG and CG regions for HS Ti-6Al-4V. The volume fraction of FG regions can be accurately controlled in the generated FE model by its 'thickness' between two neighboring CG regions. For FG regions, 50 equiaxed α grains are considered at each Gauss point and are supposed to be sufficient for the accuracy of the numerical model. The average number of lamellar α+β colonies in every CG regions can be determined by using the EBSD maps. In this simulation, 7 lamellar α+β colonies are considered for each CG region. Another important parameter which influences the accuracy of the FE model is the number of CG regions included in the RVE. Figure 13 shows three RVEs with edge length of 1mm, which

contain 30, 50 and 100 CG regions respectively and have the same volume fraction of FG regions (13.34%). Monotonic simple shear loading is applied in the FE model tests up to $\Gamma = 10.0\%$ of the overall shear strain. The numerical results shown in Figure 14 indicate that the difference between the overall responses is not significant when using the three RVEs. And the accuracy of FE models can be obtained when the number of CG regions is 50, as the overall response of RVEs including 50 CG regions is very close to that including 100 CG regions.

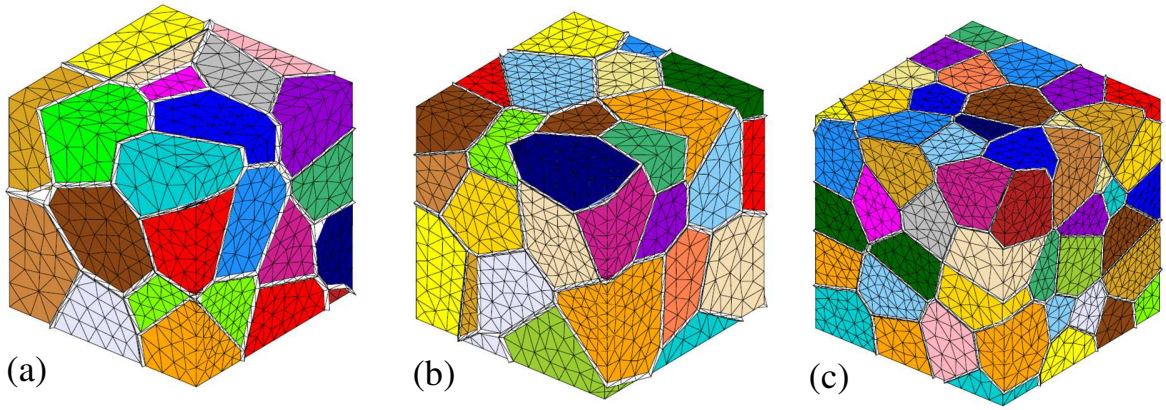

Figure 13. Illustration of RVEs including (a) 30, (b) 50 and (c) 100 CG regions for HS Ti-6Al-4V, where every colored part represents a CG region and the white part represents FG regions.

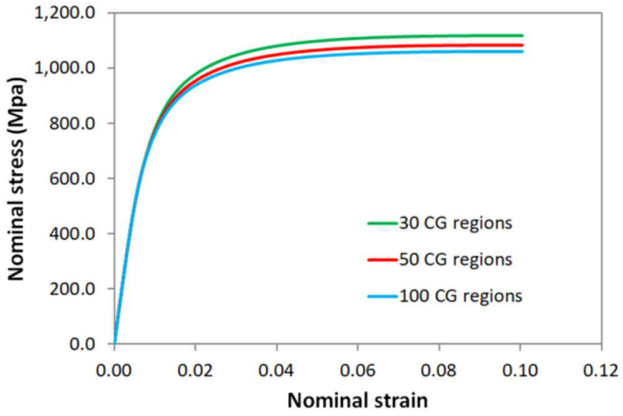

Figure 14. Effect of the number of CG regions in the FE model on the overall response of HS Ti-6Al-4V under monotonic simple shear loading condition.

5.0 Numerical results and discussions

The above developed model is used to simulate the microstructure-related mechanical behavior of homogeneous CG and HS specimens for CP-Ti and Ti-6Al-4V. Priority is given to

the representation of the numerical results on HS Ti-6Al-4V as these results cannot be found in previous literature.

5.1 Comparison with experiments for CP-Ti

The simulations of monotonous and cyclic simple shear deformation for CP-Ti with homogeneous coarse-grained and harmonic structured microstructures had been conducted in authors' previous work (Wang et al., 2019). While in this study, for the sake of using the same set of constitutive relations in simulating CP-Ti and Ti-6Al-4V properties, a flow rule which could be found in numerical works about these two materials is used. Consequently, all the simulations are newly carried out and the simulation results are qualitatively similar to those presented in (Wang et al., 2019). For the purpose of further analysis of difference in strengthening effect, the comparisons between numerical results and experimental data for monotonic shear test are presented here in brief. More details can be found by referring to (Wang et al., 2019). It's observed that the simulated overall responses for homogeneous CG and HS CP-Ti under monotonous and cyclic shear loading agree well with the experimental results in terms of the yield strength and strain hardening (Figures 15-16). The numerical model is able to capture the influence of microstructure on macroscopic properties and reproduce well the strengthening effect of harmonic structure design on CP-Ti.

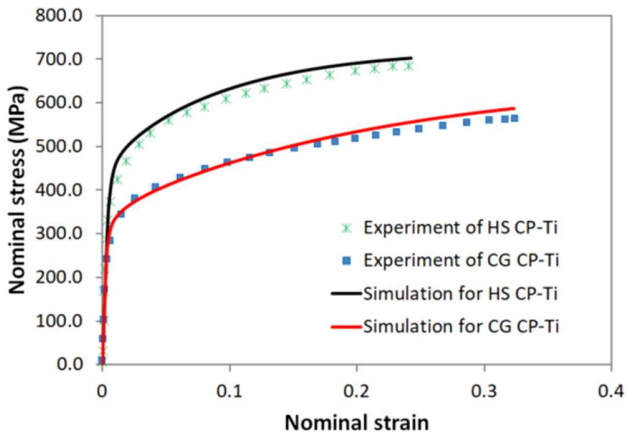

Figure 15. Simulated stress-strain curves and experimental results for homogeneous coarse-grained CP-Ti and harmonic structured CP-Ti in the case of monotonic simple shear condition.

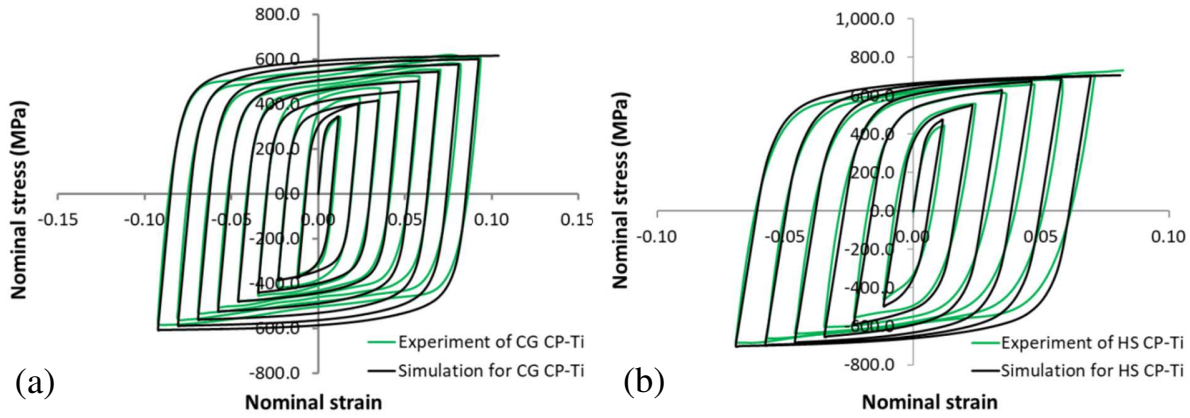

Figure 16. Simulated curves and experimental results for (a) homogeneous coarse-grained CP-Ti and (b) harmonic structured CP-Ti in the case of cyclic simple shear condition when $\Delta\Gamma = 1.155\%$ every cycle.

5.2 Comparison with experiments for Ti-6Al-4V

The monotonous and cyclic overall stress-strain responses obtained by simulations for homogeneous CG Ti-6Al-4V and HS Ti-6Al-4V using the proposed numerical model are shown in Figure 17 and Figure 18 respectively, in comparison with the experimental data. It can be noticed that there is a good agreement between the simulations and experimental results. The simulations capture well the strengthening effect of harmonic structure design on Ti-6Al-4V material, as shown in Figure 17. The cyclic hardening is also precisely reproduced by the proposed numerical model according to Figure 18. It can be remarked that the numerical model is able to describe the microstructure's influence on the macroscopic behavior of homogeneous CG Ti-6Al-4V and HS Ti-6Al-4V.

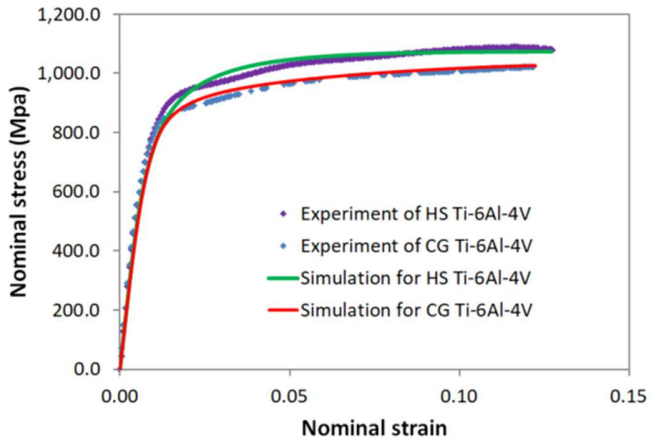

Figure 17. Comparison between simulations and experimental results for homogeneous CG Ti-6Al-4V and HS Ti-6Al-4V in the case of monotonic simple shear condition.

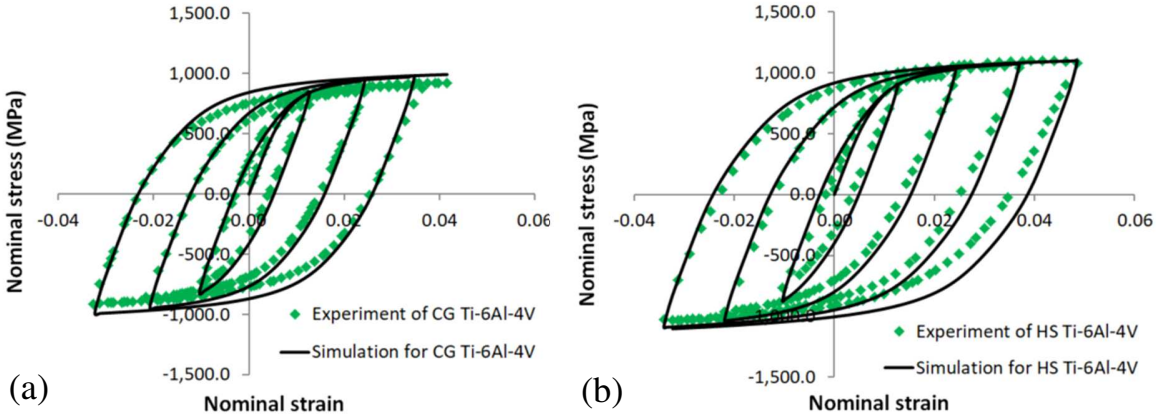

Figure 18. Simulated curves and experimental results for (a) homogeneous coarse-grained Ti-6Al-4V and (b) harmonic structured Ti-6Al-4V in the case of cyclic simple shear condition when $\Delta\Gamma = 1.155\%$ every cycle.

5.3 Comparison between Ti-6Al-4V and CP-Ti

5.3.1 Strengthening effects

Referring to experimental data (Figure 15), HS CP-Ti shows a much higher ultimate shear stress (684 MPa) compared with that of homogeneous CG CP-Ti (581 MPa). The material strength is increased by 17.7%. However, Figure 17 shows that the ultimate shear stress of Ti-6Al-4V is only augmented by 6.6%, from 1021 MPa (homogeneous CG Ti-6Al-4V) to 1088 MPa (HS Ti-6Al-4V). It's apparent that the improvement of Ti-6Al-4V's strength by applying

harmonic structure design is not as significant as that observed in CP-Ti. This phenomenon consists of the key point of discussions.

5.3.2 Comparison between HS CP-Ti and HS Ti-6Al-4V

Figure 19 displays the simulated effective shear stress distributions on the surfaces of the HS CP-Ti and HS Ti-6Al-4V RVEs in the case of monotonic shear condition when the overall strain reaches the largest imposed value. From Figure 19a, a sharp contrast of stress levels can be observed between the FG and CG regions in the harmonic structured CP-Ti RVE. The stress level in FG regions is apparently much higher than that in CG regions, which only approximates the overall stress. It can be deduced that for HS CP-Ti the strengthening effect is mainly caused by the FG regions.

As a contrasting case, the stress field in HS Ti-6Al-4V is dramatically different, as shown in Figure 19b. It can be seen that some neighboring CG regions display completely different stress levels. It appears that some CG regions are much 'harder' than the others. This phenomenon is quite different from the HS CP-Ti sample, in which stress field in the CG regions is relatively homogeneous. Moreover, no special stress concentration can be found in the FG regions. Different from the HS CP-Ti sample, no strong strengthening effect of FG regions is revealed.

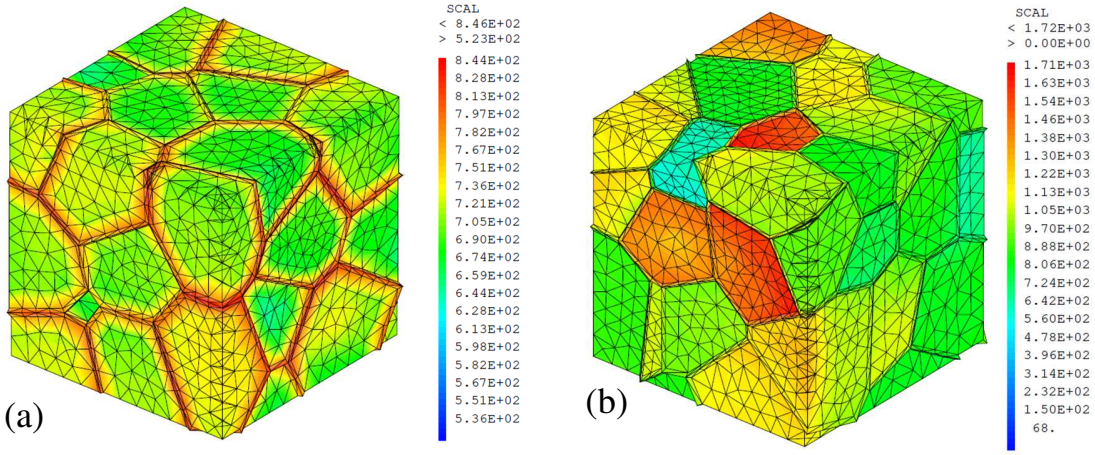

Figure 19. Effective shear stress distribution for (a) HS CP-Ti when $\Gamma = 24.0\%$ and (b) HS Ti-6Al-4V when$\Gamma = 12.7\%$.

Figure 20 displays the effective shear strain fields for HS CP-Ti and HS Ti-6Al-4V in the case of monotonic simple shear condition. For HS CP-Ti, the relatively hard FG regions tend to carry lower strains and strain concentration mainly emerges in CG regions. This feature is

especially obvious when the imposed overall strain is small, as shown in Figure 20a. This deformation behavior shown in the simulation is in agreement with experimental observations reported in (Park et al., 2018). However, for HS Ti-6Al-4V, a close inspection of Figure 20c reveals no strong correlation between the spatial arrangement of 'hard' and 'soft' CG regions and the strain distribution.

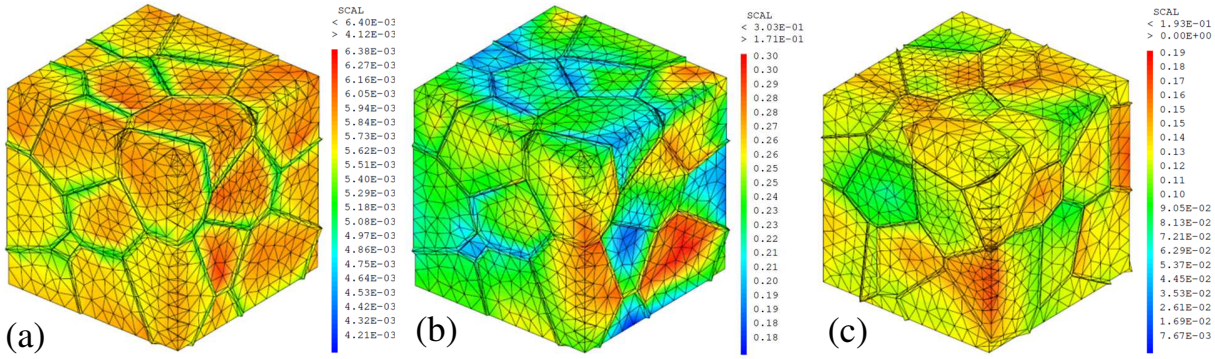

Figure 20. Effective shear strain distribution for (a) HS CP-Ti when $\Gamma = 0.57\%$, (b) HS CP-Ti when $\Gamma = 24.0\%$ and (c) HS Ti-6Al-4V when $\Gamma = 12.7\%$.

5.3.3 Comparison between CG CP-Ti and CG Ti-6Al-4V

Looking at the effective shear stress distribution for homogeneous CG CP-Ti and homogeneous CG Ti-6Al-4V in Figure 21, it can be noticed that there exists 'hard' grains (or colonies for Ti-6Al-4V) with high stress concentration neighboring with 'soft' grains (or colonies) with relatively low stress level. This arrangement of neighboring 'hard' and 'soft' grains (or colonies) inevitably creates mismatches of deformation and generates heterogeneous strain distribution among the neighboring grains (or colonies), as displayed by Figure 22.

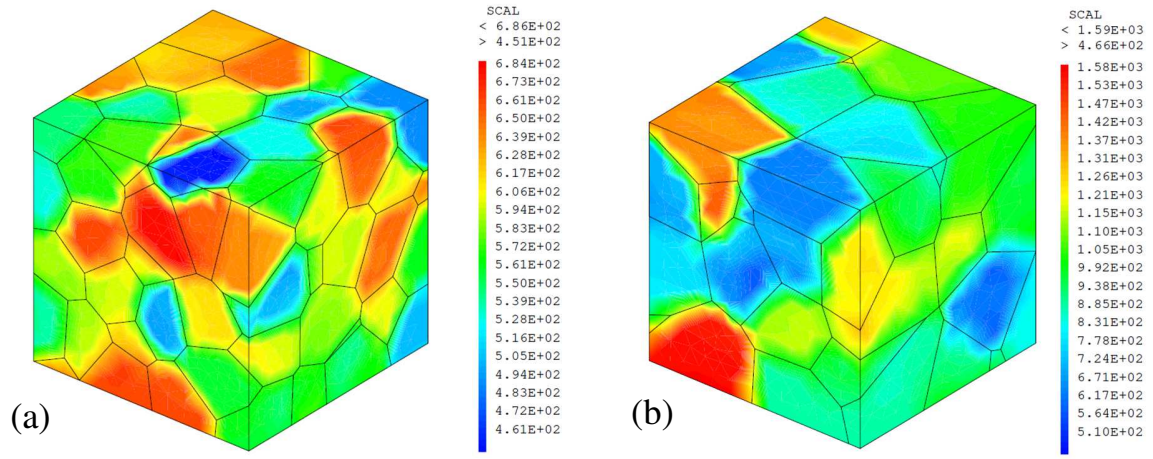

Figure 21. Effective shear stress distribution for (a) homogeneous CG CP-Ti when $\Gamma = 24.0\%$ and (b) homogeneous CG Ti-6Al-4V when $\Gamma = 12.7\%$.

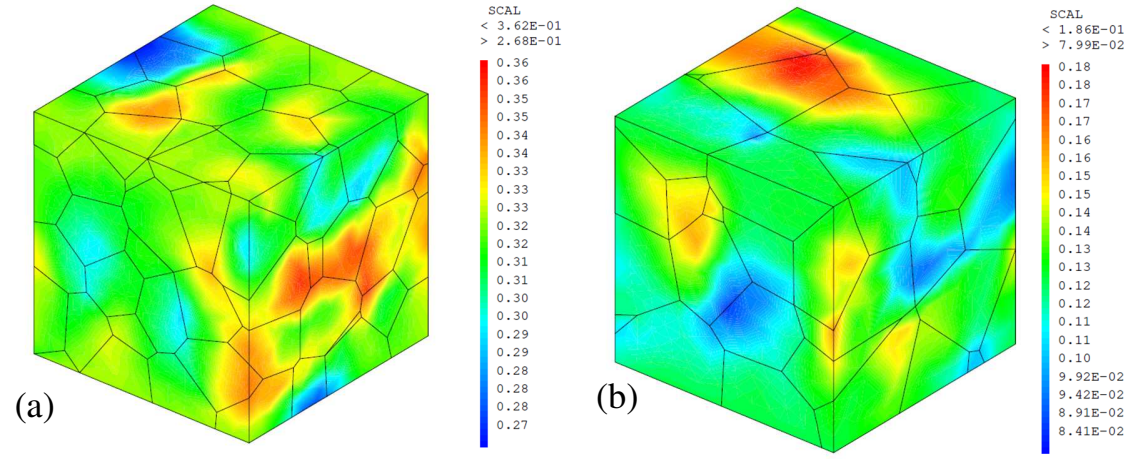

Figure 22. Effective shear strain distribution for (a) homogeneous CG CP-Ti when $\Gamma = 24.0\%$ and (b) homogeneous CG Ti-6Al-4V when $\Gamma = 12.7\%$.

5.4 Prevision for different volume fractions of FG regions

It's very challenging to change one microstructure feature without modifying the others experimentally, because the variation of these features is usually highly coupled. However, it can be convenient to vary the microstructure features independently in numerical simulations to obtain a direct insight of their effect on material properties. Thus an array of synthetic specimens is generated in this section by varying the volume fraction of FG regions in HS CP-Ti and HS Ti-6Al-4V. Then simulations are conducted to study the responses to variations in this volume fraction. It should be noted that only the volume fractions of FG and CG regions are varied while

other microstructure lengths and parameter values are held constant in the analysis. Referring to the reported ranges in previous experimental studies, volume fraction of FG regions for each synthetic specimen is fixed at 13.3%, 16.0%, 20.0% and 25.0% respectively. All the simulation results for HS CP-Ti and HS Ti-6Al-4V (Figure 23) show a positive correlation between the volume fraction of FG regions and material strength. Material strength follows a rising trend with an increase of volume fraction of FG regions in HS CP-Ti and HS Ti-6Al-4V. As mentioned in the previous comparisons, there is a greater sensitivity to changes of HS features for CP-Ti in comparison with Ti-6Al-4V.

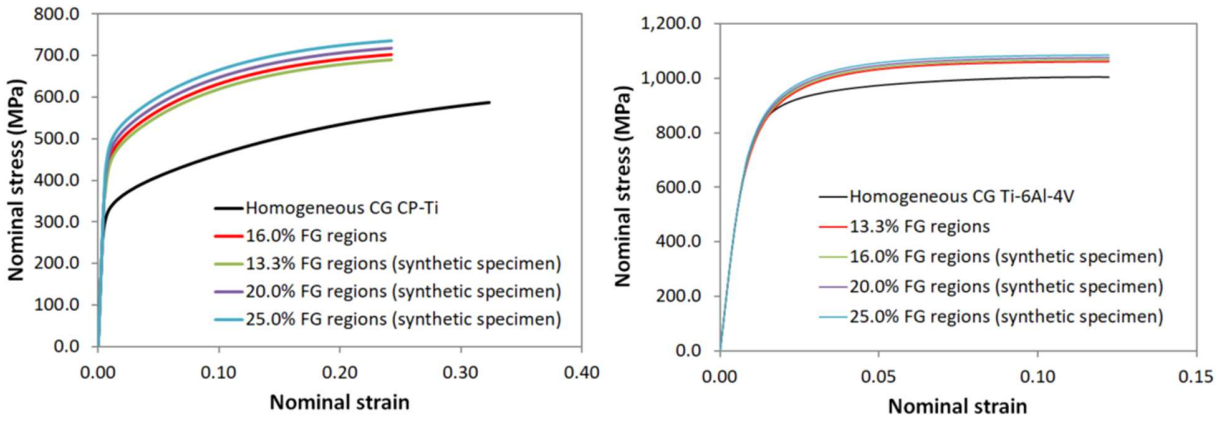

Figure 23. Simulated responses to variations in volume fraction of FG regions conducted on synthetic specimens (a) for HS CP-Ti and (b) for HS Ti-6Al-4V in comparison with simulations for experimental specimens.

5.5 Discussions on the strengthening mechanism

In the present numerical model, the length scale effect as depicted by Eq. (9) is considered as one of the main sources of strengthening effect caused by HS design, which essentially represents the obstacles formed by grain or α/β interface boundaries to dislocation motions. Another underlying source of strengthening effect is the spatial arrangement of FG and CG regions due to the HS design, which is implicitly represented through the corresponding FE meshes.

As pointed previously, the microstructure effects of the HS design on the material properties are quite different CP-Ti and Ti-6Al-4V. For HS CP-Ti, numerical studies show that the FG regions tend to perform like a thin but relatively hard skeleton enveloping the soft CG regions. Therefore, CP-Ti with HS design is able to bear higher level of external load and endure large deformation, exhibiting a higher strength without great loss of ductility.

However, the enhancement of material strength by applying HS design to Ti-6Al-4V is not as efficient as observed in the case of HS CP-Ti. This is most likely attributed to the following two facts:

(1) From the viewpoint of length scale effect, in CG regions the average size of the lamellar α+β colonies is about 50 μm. However, the mechanical properties of an individual lamellar α+β colony are not determined only by this length scale due to the special deformation mechanism caused by the lamellar α+β microstructure. When the hard deformation mode is predominant in certain cases, the widths of α and β laths (2.5 μm and 0.2 μm respectively) could have a major influence on the mechanical behavior of the lamellar α+β colony (Mayeur, 2004). Consequently, even though the average size of equiaxed α grains in FG regions is about 2 μm, the strengthening effect caused by its relatively small grain sizes is no longer as significant as in the case of HS CP-Ti.

(2) Among the 36 slips systems in a lamellar α+β colony, 6 slip systems are related to the soft deformation modes. As shown in Figure A1, they are three basal, 1 prismatic and 2 $\langle 111 \rangle \{ 110 \}$ slip systems. It can be noticed that, by obeying the Burgers orientation relationship, the distribution of these slip planes and slip directions are quite concentrated in three-dimensional space. Besides, there is a big difference between the length scales concerning the soft and hard deformation modes. Because of these two aspects, an individual lamellar α+β colony becomes significantly anisotropic. In each CG region, only 7 lamellar α+β colonies are taken into account in the numerical simulation and the grain orientation for every lamellar α+β colony is randomly generated. Therefore a CG region is very likely to be anisotropic too. When a load in a fixed direction is applied to the RVE, some CG regions become 'hard' and some other become 'soft.' Consequently, the local stress is not concentrated in FG regions. This anisotropy strengthening mechanism, which is not significant in CP-Ti, hides the strengthening effect of the FG regions.

6.0 Concluding remarks

In the present work, we proposed a multi-scale numerical model, which incorporated a crystal plasticity model and a micro-macro transition scheme, to simulate the microstructure dependent behavior of CP-Ti and Ti-6Al-4V with or without HS design. This model is successfully implemented into a three-dimensional finite element code. It is shown that experimental results can be well reproduced for homogeneous CG and HS specimens under

monotonous and cyclic simple shear loading conditions. The present study leads us to make the following concluding remarks:

1. Based on the investigations of HS CP-Ti and HS Ti-6Al-4V, a general strengthening mechanism of harmonic structure designed materials is proposed. The underlying sources of strengthening effect are mainly the length scale effect and the special arrangement of FG and CG regions. Meanwhile, the strengthening of HS materials also is directly influenced by grain orientations, the number of grains (or colonies) in CG regions and the anisotropy of slip system strength.

2. The enhancement of material strength caused by the HS design is more significant for CP-Ti than Ti-6Al-4V. For HS CP-Ti, numerical simulations clearly indicate that the strengthening is mainly caused by the FG regions, which carry an big part of external load. However, for HS Ti-6Al-4V, even the average size of equiaxed α grains in FG regions is much small compared with the lamellar α+β colony size in CG regions, the improvement of the mechanical property is not as significant as expected. The main reason βor this counter performance is the hard deformation model in lamellar α+β colonies in Ti-6Al-4V. In fact, the small microstructure lengths in lamellar α+β colonies, i.e., the widths of α and β laths, are similar to the average size of equiaxed α grains in FG regions. Therefore, the strengthening effect of FG regions is largely hidden, resulting in a slight improvement of material strength.

3. The proposed numerical model is capable of simulating deformation behavior of HS CP-Ti and HS Ti-6Al-4V. Numerical results are in good agreement with experimental data. By varying microstructure features independently in simulations, it's possible to gain a quantitative understanding of the key microstructure effects of the HS design on material properties, viz. the influence of some important parameters such as volume fractions of FG and CG regions, average size of grains or colonies, or widths of α and β laths in lamellar α+β colonies.

Acknowledgements

The support by the French National Research Agency in the framework of ANR 14-CE07-0003 "HighS-Ti" program is highly acknowledged. Xiang WANG highly acknowledges the financial support from China Scholarship Council (CSC). G. Dirras is grateful to Dr D. Tingaud and Dr. F. Mompiou for fruitful discussions regarding EBSD and EDS investigations.

References

Barbe, R.J., Decker, L., Jeulin, D., Cailletaud, G., 2001. Intergranular and intragranular behavior of polycrystalline aggregates. Part 1: F.E. model. Int. J. Plast. 17 (**4**), 513-536.

Barkia, B., 2014. Viscoplasticité à l'ambiante du titane en relation avec ses teneurs en oxygène et hydrogène. PhD thesis. Ecole Polytechnqiue.

Barton, N.R., Dawson, P.R., 2001. On the spatial arrangement of lattice orientations in hot-rolled multiphase titanium. Modell. Simul. Mater. Sci. Eng. 9, 433-463.

Brockman, R., 2003. Analysis of elastic-plastic deformation in TiAl polycrystals. Int. J. Plast. 19, 1749-1772.

Cailletaud, G., 1987. Une Approche Micromécanique Phénoménologique du Comportement Inélastique des Métaux. Thèse d'état, Univ. Paris VI.

Chaboche, J.L., 1989. Constitutive equations for cyclic plasticity and cyclic viscoplasticity. Int. J. Plast. 5, 247-302.

Cailletaud, G., Pilvin, P., 1994. Utilisation de modéles polycristallins pour le calcul par éléments finis. Rev. Eur. Eléments Finis. 3, 515-541.

Dirras, G., Ueda, D., Hocini, A., Tingaud, D., Ameyama, K., 2017. Cyclic shear behavior of conventional and harmonic structure-designed Ti-25Nb-25Zr β-titanium alloy: Back-stress hardening and twinning inhibition. Scr. Mater. 138, 44-47.

Fang, T.H., Li, W.L., Tao, N.R., Lu, K., 2011. Revealing extraordinary intrinsic tensile plasticity in gradient nano-grained copper. Sci. 331, 1578-1590.

Fujiwara, H., Tanaka, H., Nakatani, M., Ameyama, K., 2010. Effects of Nano / Meso Harmonic Microstructure on Mechanical Properties in Austenitic Stainless Steel Produced by MM / HRS Process. Mater. Sci. Forum. 1790-1795.

Goh, C.H., Wallace, J.M., Neu, R.W., McDowell, D.L., 2001. Polycrystal Plasticity Simulations of Fretting Fatigue. Int. J. Fatigue. 23, 423-435.

Goh, C.-H., Neu, R.W., McDowell, D.L., 2003. Crystallographic plasticity in fretting of Ti-6Al-4V. Int. J. Plast. 19 (**10**), 1627-1650.

Hama, T., Kobuki, A., Takuda, H., 2017. Crystal-plasticity finite-element analysis of anisotropic deformation in a commercially pure titanium Grade 1 sheet. Int. J. Plast. 91, 77-108.

Hocini, A., 2017. Étude comparative du comportement mécanique et des mécanismes de déformation sous cisaillement simple et cyclique des alliages de titane élaborés par métallurgie des poudres: structures harmoniques versus alliages conventionnels, PhD Thesis, Univ. Paris XIII.

Kang, J.Y., Kim, J.G., Kim, S.K., Chin, K.G., Lee, S., Kim, H.S., 2016. Outstanding mechanical properties of higi-pressure torsion processed multiscale TWIP-cored three layer steel sheet. Scr. Mater. 123, 122-125.

Kasemer, M., Quey, R., Dawson, P., 2017. The influence of mechanical constraints introduced by β annealed microstructures on the yield strength and ductility of Ti-6Al-4V. J. Mech. Phys. Solids. 103, 179-198.

Kikuchi, S., Kubozono, H., Nukui, Y., Nakai, Y., Ueno, A., Kawabata, M.O., Ameyama, K., 2018. Statistical fatigue properties and small fatigue crack propagation in bimodal harmonic structured Ti-6Al-4V alloy under four-point bending. Mater. Sci. Eng. A 711, 29-36.

Langlois, P., Tingaud, D., Dirras, G., 2019. Spark Plasma Sintering as a route for producing in-demand microstructures: Application to the tensile-ductility enhancement of polycrystalline nickel, In: Cavaliere, P. (Eds.), Spark Plasma Sintering of Materials. Springer, Cham, pp. 575-604.

Lu, K., 2014. Making strong nanomaterials ductile with gradients. Sci. 345, 1455-1456.

Leyens, C., Peters, M., 2003. Titanium and titanium alloys: fundamentals and applications. Wiley-VCH, Weinheim.

Lutjering, G., Williams, J.C., 2003. Titanium. Springer, New York, NY.

Liu, J., Li, J., Dirras, G., Ameyama, K., Cazes, F., 2018. A three-dimensional multi-scale polycrystalline plasticity model coupled with damage for pure Ti with harmonic structure design. Int. J. Plast. 100, 192-207.

Ma, E., Zhu, T., 2017. Towards strength–ductility synergy through the design of heterogeneous nanostructures in metals. Mater. Today. 20, 323-331.

Mayeur, J.R., 2004. Three-dimensional modeling of titanium–aluminum alloys with application to attachment fatigue. M.S. Thesis, Georgia Institute of Technology, Atlanta, GA, USA.

Mayeur, J.R., McDowell, D.L.,2007. A three-dimensional crystal plasticity model for duplex Ti-6Al-4V. Int. J. Plast. 23, 1457-1485.

Morrissey, R.J., 2001. Strain Accumulation and Shakedown in Fatigue of Ti-6Al-4V. Ph.D. Thesis, Georgia Institute of Technology.

Neeraj, T., Savage, M.F., Tatalovich, J., Kovarik, L., Hayes, R.W., Mills, M.J., 2005. Observation of tension-compression asymmetry in a and a-b titanium alloys. Phil. Mag. A 85, 279-295.

Naka, S., Lasalmonie, A., 1983. Cross-slip on the first order pyramidal plane $(10\bar{1}1)$ of atype dislocations $[12\bar{1}0]$ in the plastic deformation of α-titanium single crystals. J. Mater. Sci. 18, 2613-2617.

Naka, S., Lasalmonie, A., Costa, P., Kubin, L., 1988. The low-temperature plastic deformation of α-titanium and the core structure of a-type screw dislocations. Phil. Mag. A 57, 717-740.

Orlov, D., Fujiwara, H., Ameyama, K., 2013. Obtaining copper with harmonic structure for the optimal balance of structure-performance relationship. Mater. Trans. 54 (**9**), 1549-1553.

Ota, M., Shimojo, K., Okada, S., Vajpai, SK., Ameyama, K., 2014a. Harmonic Structure Design and Mechanical Properties of Pure Ni Compact. J. Powder Metall. Min. 3, 1-5.

Ota, M., Vajpai, SK., Imao, R., Kurokawa, K., Ameyama, K., 2014b. Application of High Pressure Gas Jet Mill Process to Fabricate High Performance Harmonic Structure Designed Pure Titanium. Mater. Trans. 1-6.

Obstalecki, M., Wong, S.L., Dawson, P.R., Miller, M.P., 2014. Quantitative analysis of crystal scale deformation heterogeneity during cyclic plasticity using high-energy X-ray diffraction and finite-element simulation. Acta Mater. 75, 259-272.

Pilvin, P., 1990. Approaches Multiéchelles pour la Prévision du Comportement Inélastique des Métaux. PhD thesis, Univ. Paris VI.

Park, H.K., Ameyama, K., Yoo, J., Hwang, H., Kim, H.,S., 2018. Additional hardening in harmonic structured materials by strain partioning and back stress. Mater. Res. Lett. 6, 261-267.

Simmons, G., Wang, H., 1971. Single Crystal Elastic Constants and Calculated Aggregate Properties: A Handbook. The MIT Press, Cambridge, MA.

Seagle, S.R., 1997. Titanium and titanium alloys. Kirk-Othmer Encyle. Chem. Technol. 24, 2.

Song, X., Zhang, S.Y., Dini, D., Korsunsky, A.M., 2008. Finite element modelling and diffraction measurement of elastic strains during tensile deformation of HCP polycrystals. Comput. Mater. Sci. 44, 131-137.

Suri, S., Viswanathan, G.B., Neeraj, T., Hou, D.H., Mills, M.,1999. Room temperature deformation and mechanisms of slip transmission in oriented single-colony crystals of an α/β titanium alloy. Acta Metall. 47, 1019-1034.

Schoenfeld, S.E., Kad, B., 2002. Texture Effects on Shear Response in Ti-6Al-4V Plates. Int. J. Plast. 18, 461-486.

Tingaud, D., Sadat, T., Dirras, G., 2019. Nickel-Tungsten Composite-Like Microstructures Processed by Spark Plasma Sintering for Structural Applications, In: Cavaliere P. (Eds), Spark Plasma Sintering of Materials. Springer, Cham, pp. 605-634.

Vajpai, S.K., Yu, H., Ota, M., Watanable, I., Dirras, G., Ameyama, K., 2016a. Three-dimensionally gradient and periodic harmonic structure for high performance advanced structural materials. Mater. Trans. 57, 1424-1432.

Vajpai, S.K., Sawangrat, C., Yamaguchi, O., Ciuca, O.P., Ameyama, K., 2016b. Effect of bimodal harmonic structure design on the deformation behavior and mechanical properties of Co-Cr-Mo alloy. Mater. Sci. Eng. C. 58, 1008-1015.

Wang, X., Cazes, F., Li, J., Hocini, A., Ameyama, K., Dirrsa, G., 2019. A 3D crystal plasticity model of monotonic and cyclic simple shear deformation for commercial-purity polycrystalline Ti with a harmonic structure. Mech. Mater. 128, 117-128.

Yang, Y., Wang, L., Zambaldi, C., Eisenlohr, P., Barabash, R., Liu, W., Stoudt, M.R., Crimp, M.A., Bieler, T.R., 2011. Characterization and modeling of heterogeneous deformation in commercial purity titanium. JOM. 63, 66-73.

Zhang, Z., Vajpai, S.K., Orlov, D., Ameyama, K., 2014. Improvement of mechanical properties in SUS304L steel through the control of bimodal microstructure characteristics. Mater. Sci. Eng. A. 598, 106-113.

Zhang, M., Zhang, J., McDowell, D.L., 2007. Microstructure-based crystal plasticity modeling of cyclic deformation of Ti-6Al-4V. Int. J. Plast. 23 (**8**), 1328-1348.

Zheng, R., Zhang, Z., Nakatani, M., Ota, M., Chen, X., Ma, C., Ametama, K., 2016. Enhanced ductility in harmonic structure designed SUS316L produced by high energy ball milling and isostatic sintering. Mater. Sci. Eng. A. 674, 212-220.

Appendix 1: Microstructural aspect of the equivalent constitutive model

In this Appendix, the microstructure aspect of the equivalent constitutive model (ECM) is briefly presented in order to make the paper more self-consistent. More complete description of the ECM concept can be found in the original papers of Mayeur et al. (2004, 2007) and Zhang et al. (2007).

A1: Microstructure of a lamellar α+β colony

Ti-6Al-4V alloy possess a complex microstructure essentially characterized by the lamellar α+β colonies containing secondary α and β phases arranged in lamellar structure. There are 24

different slip systems in the α phase and 12 slip systems in the β phase. The slip systems in the α+β lamella are listed in Table A1.

Table A1

Slip systems used in this study.

Phase	Crystal type	Slip families	Indices	Number of slip systems
α	HCP	Basal	$\{0001\}11\bar{2}0$	3
α	HCP	Prismatic	$\{1010\}\bar{1}1\bar{2}0$	3
α	HCP	Pyramidal <a>	$\{1011\}\bar{1}1\bar{1}0$	6
α	HCP	Pyramidal <a+c>/A	$\{01\bar{1}1\}2\bar{1}\bar{1}\bar{3}$	12
β	BCC	-	$\{110\}111$	12

A2: Burgers orientation relation (BOR)

The crystallographic orientation of the α and β lamellae in lamellar α+β colonies are strictly coupled to each other obeying the Burgers orientation relationship (Lutjering and Williams, 2003; Suri et al., 1999). These relationships are as follows: $(0\ 0\ 0\ 1)_\alpha$ // $\{1\ 1\ 0\}_\beta$ and $<1\ 1\ \bar{2}\ 0>_\alpha$ // $<1\ 1\ 1>_\beta$ as shown in Figure A1a.

A3: Equivalent constitutive model (ECM)

Thanks to the special microstructure of the α+β colonies and the Burgers orientation relation, the entire laminar α+β colony can be considered as a single super grain in the crystal plasticity analysis (Figure A1b). Inspired by the notion in the work of Goh et al. (2003), Mayeur (2004) assumed that slip systems having a slip direction intersecting the α/β interfaces are difficult to activate because of the comparatively short effective slip distance. And the threshold stresses of these slip systems belonging to the HCP slip systems and BCC slip systems are governed by α lath width and the β rib width respectively through a Hall-Petch type relation. On the contrary, slip systems which slide parallel to the phase interfaces or bear parallel slip planes in two phases are not affected by the interfaces' obstacles to slip transmission. These soft slip systems consist of three basal, one prismatic and two $\langle 111\rangle\{110\}$ slip systems. The corresponding threshold stresses of these soft slip systems are not governed by the microstructural length scales as the hard slip systems.

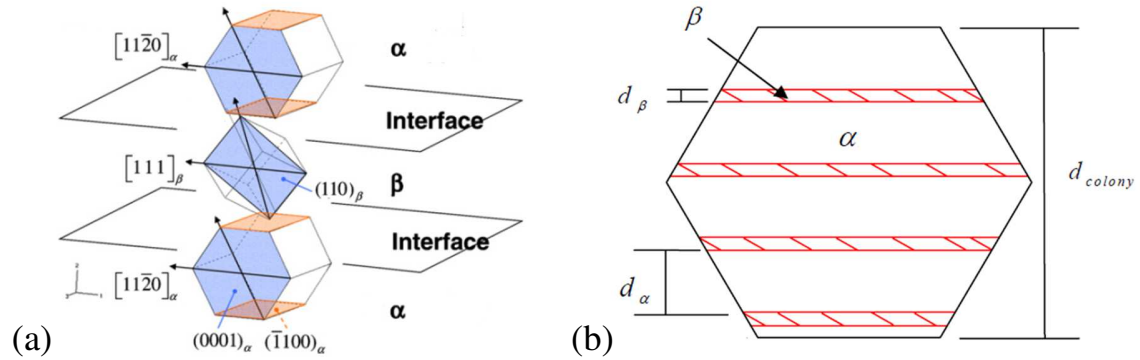

Figure A1. Schematic illustrating (a) Burgers orientation relationship in lamellar α+β colonies and (b) lamellar colony length scales (Zhang et al., 2007).